Nanoscale

Accepted Manuscript

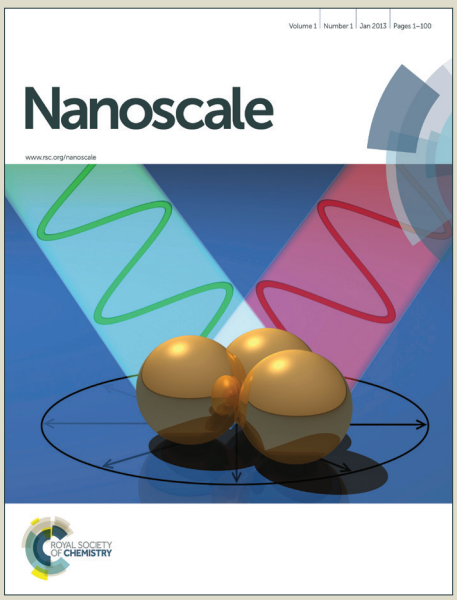

ROYAL SOCIETY OF CHEMISTRY

www.rsc.org/nanoscale

Nanoscale

COMMUNICATION

A Novel Nanoporous Fe-doped Lithium Manganese Phosphate Material with Superior Long-term Cycling Stability for Lithium-ion Batteries

Received 00th January 20xx,
Accepted 00th January 20xx

DOI: 10.1039/x0xx00000x

www.rsc.org/

Pengjian Zuo*[a], Liguang Wang[a], Wei Zhang[a], Geping Yin[a], Yulin Ma[a], Chunyu Du[a], Xinqun Cheng[a], Yunzhi Gao[a]

Here, we prepared $LiMn_{0.8}Fe_{0.2}PO_4$ microspheres with an open three-dimensional nanoporous structure by a facile ion-exchange solvothermal method. The micro/nano-structured material exhibits an ultralong cycle life, and remains a reversible capacity of 105 mAh·g^{-1} after 1000 cycles at 5 C, corresponding to the capacity retention of 94.0% and only 0.0068 mAh·g^{-1} loss per cycle.

Since the pioneering studies of Goodenough and co-workers, $LiMPO_4$ materials (M = Fe, Mn, Co, or Ni) with a theoretical capacity of around 170 mAh·g^{-1} have been investigated as promising cathode materials for lithium ion batteries owing to their appealing features including the excellent thermal stability, environmental friendliness and low cost.[1-3] However, $LiMPO_4$ materials have intrinsically poor electrical and ionic conductivity which influences their electrochemical performances.[4] Among these materials, carbon-coated $LiFePO_4$ (LFP) with an improved electric conductivity of about 10^{-1} S·cm^{-1} at room temperature has already been commercialized successfully.[5, 6] The great success of LFP brings impulsion moving to $LiMnPO_4$ (LMP) due to its higher energy density related to Mn^{2+}/Mn^{3+} redox potential (4.1 V *vs.* Li^+/Li) in comparison with the Fe^{2+}/Fe^{3+} redox potential (3.4 V *vs.* Li^+/Li).[7-9] However, LMP suffers from intrinsic drawbacks of extremely low electronic conductivity ($<10^{-10}$ S·cm^{-1}, compared with 1.8×10^{-8} S·cm^{-1} for LFP)[10], high surface energy barrier for lithium diffusion at the surface[11], a large kinetic barrier to ion and electron hopping at the phase boundary resulting from the Jahn-Teller distortion and meta-stability of the delithiated phase.[12-14]

To improve the electrochemical performance of LMP, many strategies similar to the modifications of LFP mainly focused on (i) particle size reduction[15, 16], which shortens the diffusion length for lithium ion transport and also increases the effective surface area;[17, 18] (ii) surface coating with electronically conductive materials (such as carbon, conductive polymer, etc.)[9, 19, 20], and (iii) cation doping.[21, 22] S. M. Oh et al synthesized the LMP material with the size of 10-50 nm by ultrasonic spray pyrolysis followed by ball milling, and this material achieved a discharge capacity of 158 mAh·g^{-1} at the rate of C/20 with the capacity retention of 88% after 50 cycles.[23] V. Ramar et al reported an Fe^{2+} and Mg^{2+} co-doped LMP material with an individual particle size in the range of 20–40 nm delivering a discharge capacity of 159 mAh·g^{-1} at 0.1 C with a capacity retention of 96% of the initial capacity after 200 cycles at 1 C.[24] More recently, X. Zhou et al improved the rate performance of $LiMn_{0.5}Fe_{0.5}PO_4$/C material by a surfactant-assisted solid state method, and this material with the primary particle size of 35-70 nm exhibited 155 mAh·g^{-1} at 0.1 C and showed stable cycling stability (90.8% capacity retention after 500 cycles at 5 C).[25]

Although much improvement on the performance of LMP cathode has been achieved, the nanosized LMP cathode with high reversible capacity has the relatively poor long-term cyclability, which is partial related to the interface side reaction caused by the high specific surface area of the nanosized particles.[15, 26-28] Therefore, it is believed that the sphere structure cathode material with a moderate particle size possesses an appropriate active specific surface area resulting in a long-term cycle stability. In this regard, the LMP microsphere powders with a three-dimensional (3D) architecture are highly desired for developing high performance lithium ion batteries. Although some micro/nano-structure LMP materials have been reported, few of them exhibited the excellent cycling performance (over 500 cycles) to meet the demand of commercialization.[28, 29] It has been reported that Fe-doped $LiMnPO_4$ materials have revealed the impressively improved electrochemical performance.[26] Specifically, $LiMn_{0.8}Fe_{0.2}PO_4$ (LMFP), possessing relatively high operating voltage, has been widely investigated as cathode for high energy lithium ion battery.[30]

Herein, we report a facile ion-exchange solvothermal approach to synthesize hierarchical LMFP hollow microspheres consisting of primary nanoparticles with an open 3D mesoporous structure. The LMFP electrode exhibits an ultralong cycle life, and still remains a reversible capacity of about 105 mAh·g^{-1} after 1000

[a] *School of Chemical Engineering and Technology, Harbin Institute of Technology, No.92 West-Da Zhi Street, Harbin 150001, China. E-mail: zuopj@hit.edu.cn, zuopjhit@gmail.com (P. Zuo).*

† Footnotes relating to the title and/or authors should appear here.
Electronic Supplementary Information (ESI) available: SEM images of Li_3PO_4 obtained under different pH value. SEM images of Li_3PO_4 obtained by different time. SEM image of nano-LMFP/C/G. The intensity maps of HRTEM image. Nitrogen sorption isotherm and pore size distribution of nano-LMFP/C/G. TG curves of HNM-LMFP/C/G and Nano-LMFP/C/G. The first three cycles cyclic voltammetry (CV) curves of HNM-LMFP/C/G. Initial charge/discharge curves of nano-LMFP/C/G. See DOI: 10.1039/x0xx00000x

charge/discharge cycles at 5 C, corresponding to the capacity retention of 94.0% and only 0.0068 mAh·g^{-1} capacity loss per cycle.

Figure 1 illustrates the synthesis schematic of hollow-structured nanoporous LMFP material (HNM-LMFP) and the structure evolution from Li_3PO_4 hollow sphere to LMFP by the crystal structure model. This unique architecture was obtained by designing a hollow-structured mesoporous precursor of Li_3PO_4 via a modified precipitation method.[31] The formation and size of Li_3PO_4 spheres can be controlled by changing the pH values of the solution and the reaction time as shown in Figure S1 and S2. The HNM-LMFP was synthesized by a facile ion exchange process in ethylene glycol solvent. The structure evolution from Li_3PO_4 to LMFP is illustrated by the crystal structure model in Figure 1. This reaction process can be described by the following Equation 1:

$$Li_3PO_4 + M^{2+} \longrightarrow LiMn_{1-x}Fe_xPO_4 + 2Li^+ \quad (1)$$

A conductive amorphous carbon layer deriving from the pyrolyzed phenolic resin was coated onto the HNM-LMFP nanoparticles by an impregnating–drying–sintering procedure in order to compensate the poor intrinsic conductivity of LMP cathode materials. Furthermore, the as-prepared HNM-LMFP/C powders were blended with graphene to form a final composite (HNM-LMFP/C/G) by an ultrasonic dispersion process forming the 3D conductive network to further enhance the conductive contact of the nanoparticles. For comparison, the nano-LMFP/C/G composites were obtained by directly ball-milling the HNM-LMFP/C/G materials to destruct the hollow nanoporous structure (Figure S3).

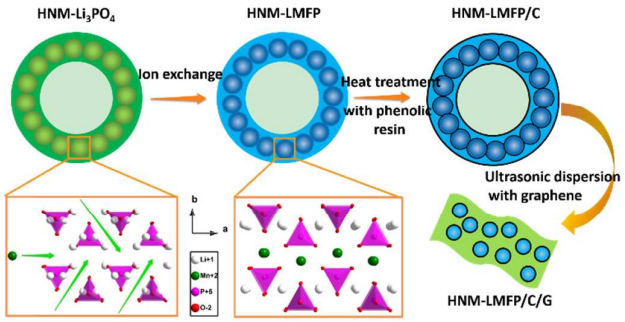

Figure 1. Synthesis schematic of HNM-LMFP/C/G and illustrating the structure evolution from Li_3PO_4 hollow sphere to LMFP by the crystal structure model.

The Li_3PO_4 precursor with a particle size of about 1 μm shows a perfect spherical structure, as shown in Figure 2a. It can be seen that these microspheres are composed of primary nanoparticles interlacing together with an open porous structure (inset, Figure 2a). The inset TEM image also shows that the Li_3PO_4 precursor has a perfect hollow structure. After the ion exchange process for preparing the LMFP particles, the porous spherical structure of HNM-Li_3PO_4 is well maintained (inset, Figure 2b). Such a hierarchical porous structure is expected to facilitate electrolyte penetration into the electrode particles, thus providing more active interface region between the electrode material and the electrolyte.[32] The nano-LMFP/C/G has a very low tap density of 0.3 g·cm^{-3}, while the tap density of the HNM-LMFP/C/G (0.9 g·cm^{-3}) is three times higher than that of the nano-LMFP/C/G sample. Figure 2c shows the TEM images of LMFP/C/G particles, and it can be seen that LMFP/C/G particle still maintains the nanoporous structure deriving from the interconnecting LMFP/C microspheres on the graphene sheet. The primary nanospherical LMFP particles with a diameter of *ca.* 30 nm are coated with a uniform thin layer of amorphous carbon (*ca.* 2 nm thick) as shown in Figure 2d. The small primary particles can provide a fast reaction and ionic diffusion kinetics during charge-discharge process. The regular lattice fringe (Figure 2d, e) and ordered bright spots (Figure 2f) show that the LMFP particles have a high crystallinity (Figure S4), which is beneficial for improving the Li^+ transport capability and enhancing the rate performance of the LMFP cathode materials.

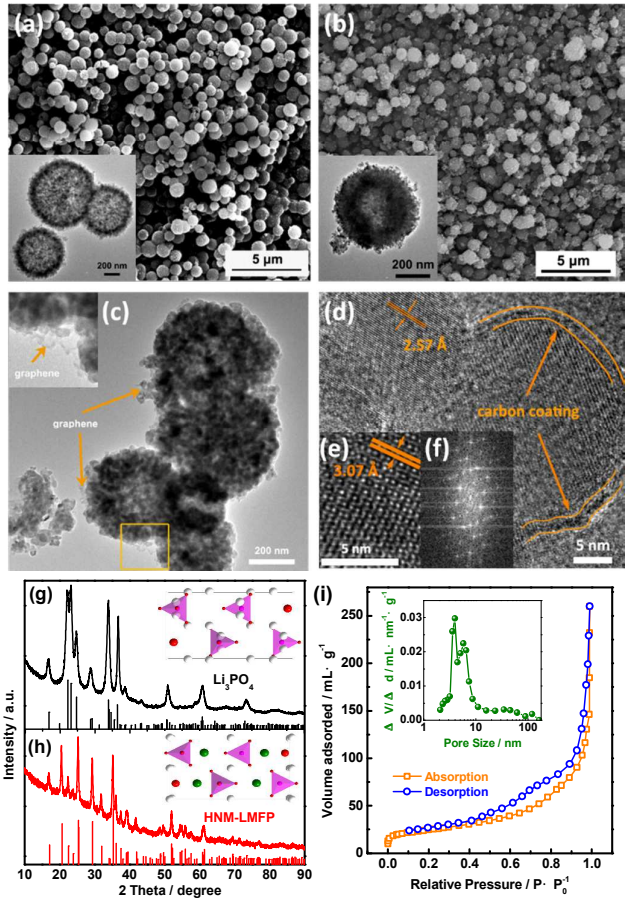

Figure 2. SEM images of (a) precursor HNM-Li_3PO_4 and (b) HNM-LMFP. The insets are the corresponding TEM images. (c)TEM and (d) HRTEM image of LMFP/C/G; the magnified of yellow square is shown in inset of (c); the interplanar spacing of 2.57 Å refers to the crystallographic directions of (131). Insets are (e) the magnified HRTEM image and corresponding Fast Fourier Transform (FFT) patterns; the interplanar spacing of 3.07 Å refers to the crystallographic directions of (121) and (200). XRD patterns of (g) precursor HNM-Li_3PO_4 and (h) HNM-LMFP. The insets are the corresponding crystal structures. The white, pink, green, and red spheres are the Li, P, Mn, and O atoms, respectively. (i) Nitrogen sorption isotherm with pore size distribution (inset) of HNM-LMFP/C/G.

Figure 2g shows that all the XRD peaks of Li_3PO_4 precursor can be indexed to a pure orthorhombic phase with space group *Pmnb*

(JCPDS No. 74-0358)[31] and no impurity phases can be detected. All the diffraction patterns of HNM-LMFP can be clearly indexed to the orthorhombic space group *Pmnb* (JCPDS No. 74-0375)[33] as shown in Figure 2h, indicating that the HNM-LMFP sample exhibits the similar crystal structure to Li_3PO_4 precursor. The homoplastic structure enables the ion exchange process by dislodging lithium atoms from Li_3PO_4 and embedding manganese atoms in the lattice to form the LMFP as illustrated in the inset of Figure 2g and h. Figure S3a shows the phase transformation process from Li_3PO_4 to LMFP after solvothermal treatment at 180℃ for different times (0-4 h). Therefore, it is believed that the ion exchange process can avoid the morphology destruction caused by the conventional dissolution-recrystallization solvothermal process.

Figure 2i and S5 show the nitrogen adsorption–desorption isotherms and the corresponding Barret-Joyner-Halenda (BJH) pore size distribution of HNM-LMFP/C/G and nano-LMFP/C/G, respectively. The adsorption isotherm for the nano-LMFP/C/G is a type III curve as shown in Figure S5, indicating a macroporous characteristic.[34] However, the HNM-LMFP/C/G displays a type IV adsorption-desorption isotherm with H3-type hysteresis as shown in Figure 2i, indicating a feature of mesoporous material. The measured Brunauer-Emmett-Teller (BET) area for nano-LMFP/C/G and HNM-LMFP/C/G is 150.5 and 84.8 $m^2 \cdot g^{-1}$, respectively. The average pore diameter of HNM-LMFP/C/G is 14.8 nm which is calculated from desorption branch of the nitrogen isotherm with the BJH method, and the corresponding BJH desorption cumulative pore volume is 0.419 $cm^3 \cdot g^{-1}$. For the nano-LMFP/C/G, the average pore diameter and the corresponding BJH desorption cumulative pore volume are 3.49 nm and 0.15 $cm^3 \cdot g^{-1}$, respectively. It's reasonable that the nano-LMFP/C/G material possesses a higher BET surface area than HNM-LMFP/C/G according to the synthesis methods of the two kinds of materials.

As mentioned above, the large contact area between the nanometer-sized particles and the electrolyte leads to the undesired side reactions, resulting in poor cycling performance and safety hazard. From this point of view, the HNM-LMFP/C/G with a hierarchical porous structure and a moderate specific surface area is expected to provide an excellent performance in lithium ion batteries. To confirm this prevision, we compared its electrochemical response with that of nano-LMFP/C/G electrode. The discharge curves of LMFP/C/G (with 8 wt% carbon, as shown in Figure S6) demonstrate a reversible potential plateau of around 4.0 V and a slightly inclined potential plateau at 3.5 V at 0.1 C (Figure 3a), which correspond to the Mn^{3+}/Mn^{2+} and Fe^{3+}/Fe^{2+} redox reactions, respectively.[35, 36] It should be mentioned that there is an abnormal increase of the potential at the initial stage in the discharge curves at 30 C and 40 C. The initial low potential may be mainly related to the charging process of the capacitor element in the charge/discharge machine at high discharge current. The decreasing potential peak spacing (ΔE_p) on the CV curves of HNM-LMFP/C/G (Figure S7) indicates that the polarization of the electrode shrinks in the first three cycles, corresponding to the activation process resulting from the insufficient lithiation/delithiation during the initial cycles.[37] The electrochemical performances of HNM-LMFP/C/G and nano-LMFP/C/G are shown in Figure 3b, c, and d. Compared with nano-LMFP/C/G (Figure S8), the specific capacity of HNM-LMFP/C/G is greatly improved at rates ranging from 1 C to 40 C, especially at higher current rates (Figure 3b). The reversible specific capacity of HNM-LMFP/C/G remains 108, 104, 81, 67, and 52 $mAh \cdot g^{-1}$ at the charge/discharge rates of 5 C, 10 C, 20 C, 30 C, and 40 C respectively. Even no any decay of the specific capacity for HNM-LMFP/C/G can be seen even after 400 cycles at 1 C, while nano-LMFP/C/G only remains 83 $mAh \cdot g^{-1}$ after 50 cycles (Figure 3c). The rate performances of HNM-LMFP/C/G compared with nano-LMFP/C/G are shown in Figure 3d. After 75 cycles, the HNM-LMFP/C/G electrode can completely revert back to the initial capacity at 0.1 C, which is much better than those of nano-LMFP/C/G (only 74.6% of the capacity in the first cycle is maintained). The excellent rate and cycling performances of HNM-LMFP/C/G cathode material may be attributed to three aspects: (i) a fast reaction and ionic diffusion kinetics due to the nanometer-scale primary Fe-doped lithium manganese phosphate crystals; (ii) the good electronic contact through the 3D conductive network formed by the amorphous carbon on the LMFP surface and the conductive graphene sheet; (iii) the well-crystallized primary nanocrystals and the structural stability of LMFP microspheres.

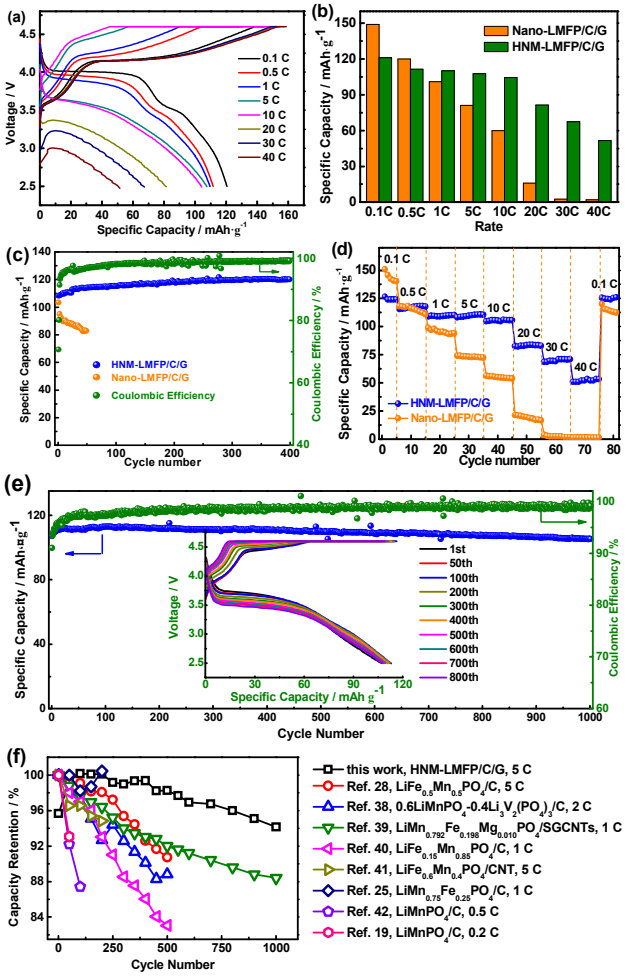

Figure 3. (a) The initial charge/discharge curves of HNM-LMFP/C/G and (b) the initial capacities compared with nano-LMFP/C/G. The cells discharged at the rate of 30 C and 40 C were also charged at 0.1 C. (c) The cycling performance of HNM-LMFP/C/G and nano-

LMFP/C/G at the rate of 1 C. (d) The rate performance of HNM-LMFP/C/G and nano-LMFP/C/G. (e) Long cycling performance of HNM-LMFP/C/G and the corresponding coulombic efficiency at the rate of 5 C. Inset is charge-discharge curves at different cycles from 1st to 800th. Each cell was charged at a certain rate to 4.6 V, kept at 4.6 V for 30 min, and then discharged at a certain rate to 2.5 V. (f) Comparison of cycling performance with other research group in the last three years. The SGCNTs in Ref. 39 is supergrowth (single-walled) carbon nanotubes, and CNT in Ref. 41 is carbon nanotubes. The different discharge rates are also labelled.

To further demonstrate the remarkable cycling stability of the HNM-LMFP/C/G electrode, we cycled the Li/ HNM-LMFP/C/G cells up to 1000 cycles under a relatively high charge/discharge rate of 5 C (Figure 3e). The specific capacity increases gradually up to the maximum of about 112 mAh·g^{-1} at the 25th cycle, and the discharge capacity of 112 mAh·g^{-1} is well maintained without any capacity loss within 200 cycles for the Li/HNM-LMFP/C/G cell. The reversible specific capacity of HNM-LMFP/C/G material decreases to 110 mAh·g^{-1} after 500 cycles, corresponding to the capacity retention of 98.4% compared with the capacity maximum of 112 mAh·g^{-1}. The HNM-LMFP/C/G cathode shows a capacity decay of 0.0036 mAh·g^{-1} per cycle in the first 500 cycles. After 1000 cycles, the discharge capacity of the HNM-LMFP/C/G cell still remains 105 mAh·g^{-1}, corresponding to the capacity retention of 94.0% and a capacity loss per cycle of only 0.0068 mAh·g^{-1}. In addition, the charge/discharge curves at different cycles from 1st to 800th are shown in the inset of Figure 3e. It should be mentioned that the polarization is not changed in the first 100 cycles. However, the electrochemical polarization is increased with the increasing cycles after the 200th cycle. The increased polarization can cause the capacity fading during long-term cycling especially at relatively high charge/discharge rate. We have compared the long-term cycle performance with that of other groups in the last three years as shown in Figure 3f.[19, 25, 28, 38-42] Moreover, the HNM-LMFP/C/G electrode shows a good structure stability after long-term cycling even at a relatively high charge/discharge rate as shown in Figure S9. To our best of knowledge, the cycling performance of HNM-LMFP/C/G in this paper is the best long-term cyclablity for the lithium manganese phosphate cathode materials till now. It can be seen clearly that the capacity retention of HNM-LMFP/C/G is much higher than that of reported materials during cycling. Actually few reported the materials exhibiting an ultralong cycle life of over 1000 cycles. Although the $LiMn_{0.792}Fe_{0.0198}Mg_{0.010}PO_4$/SGCNTs composite in Ref. 39 cycled over 1000 cycles, this cathode composite contained too much inactive single-walled carbon nanotubes (30 wt%) and just delivered a discharge capacity of 82 mAh·g^{-1} at the discharge rate of 1 C.

The electrochemical impedance spectroscopy (EIS) measurement for the Nano-LMFP/C/G and HNM-LMFP/C/G electrodes was performed in order to better understand the superior cycling performance of the cathode materials. The EIS curves shown in Figure S10 are composed of a depressed semicircle in the high-frequency region and a straight sloping line in the low-frequency region, which can be assigned to the charge-transfer process and the semi-infinite Warburg diffusion process, respectively. It can be seen that the charge-transfer resistance of HNM-LMFP/C/G electrode is much lower than that of Nano-LMFP/C/G, indicating a higher electronic conductivity and faster electrochemical reaction for the HNM-LMFP/C/G electrode. The apparent diffusion coefficient D of Li^+ is also calculated from the inclined line in the Warburg region (Figure S10b). The D value of HNM-LMFP/C/G (5.9×10^{-14} cm^{-2}·S^{-1}) is also much higher than that of Nano-LMFP/C/G (4.2×10^{-15} cm^{-2}·S^{-1}). Therefore, the HNM-LMFP/C/G also shows a higher Li^+ diffusion capability, further demonstrating its faster kinetics and excellent electrochemical performance. To understand the raising polarization of the HNM-LMFP/C/G electrode during cycling, the cell was disassembled and the cycled electrode was investigated by FTIR (Figure 4). In olivine-type materials, the PO_4 tetrahedron will be affected by the surrounding MnO_6 and LiO_6 octahedrons.[43] Hence, the structure changes of LMFP crystals can be detected by the shift of the vibration frequencies of P-O bonds from the FTIR curves.[44] After cycling, the vibration frequencies of P-O bonds shift from 975.7 cm^{-1} to 978.7 cm^{-1}. The increasing defect concentration related to the slight red shift will raise the polarization of the electrode, which is mainly resulted from the Jahn-Teller effect of Mn^{3+} in the charged state ($MnPO_4$).[12, 45-47] Therefore, the Jahn-Teller distortion is still a significant problem of the olivine-type LMP materials, which we are studying on to further improve the electrochemical performance. Moreover, the peak at 1745.3 cm^{-1} originates from C=O asymmetric stretching vibrations of RCOOLi, which is formed by electrolyte decomposition at the high voltage in the charge process. Hence, finding an electrolyte that can be stabilized in high operation voltage would be another way to enhance the electrochemical performance of the lithium manganese phosphate materials.

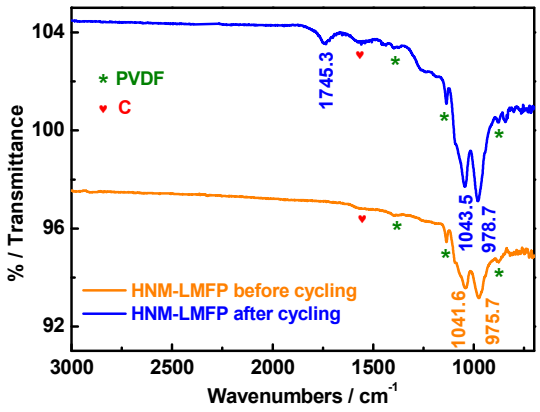

Figure 4. FTIR curves of HNM-LMFP electrodes before cycling and after 1000 cycles. The asterisk (*) and heart (♥) are the absorption peaks of PVDF and coating carbon, respectively.

Conclusions

In summary, the hollow-structured nanoporous LMFP materials were obtained using a facile ion exchange solvothermal method from hollow microspherical Li_3PO_4 precursor. This hollow microsphere architecture provides the interconnected open mesopores that facilitate the homogeneous carbon coating and electrolyte infiltration,

enhancing the electronic conductivity and reducing the diffusion path of the lithium ions. This composite delivers a discharge capacity of 110, 108, 104, 81, 67, and 52 $mAh \cdot g^{-1}$, at 1 C, 5 C, 10 C, 20 C, 30 C, and 40 C, respectively. The HNM-LMFP/C/G nano-composite exhibits a superior long-term cycling performance. After 1000 charge/discharge cycles at 5 C, the sample still remains a reversible capacity of about 105 $mAh \cdot g^{-1}$, corresponding to the capacity retention of 94.0% and only 0.0068 $mAh \cdot g^{-1}$ capacity loss per cycle compared to the maximum discharge capacity of 112 $mAh \cdot g^{-1}$. This slight capacity fading can be attributed to the structure changes caused by Jahn-Teller distortion of Mn^{3+} and the electrolyte decomposition. This novel structure can be extended to obtain various porous hierarchical materials (e.g. $LiVPO_4$, $NaMn_{1-x}Fe_xPO_4$) for application in energy storage and conversion.

Acknowledgements

This work was partially supported by The Natural Science Foundation of China (no. 50902038), National High Technology Research and Development Program (863 Program) of China (no. 2012AA110203) and Heilong Jiang Postdoctoral Funds for Scientific Research Initiation (no. LBH-Q12084).

Notes and references

‡ Footnotes relating to the main text should appear here. These might include comments relevant to but not central to the matter under discussion, limited experimental and spectral data, and crystallographic data.

1. A. K. Padhi, K. S. Nanjundaswamy and J. B. Goodenough, *J. Electrochem. Soc.*, 1997, **144**, 1188.
2. D. Choi, J. Xiao, Y. J. Choi, J. S. Hardy, M. Vijayakumar, M. S. Bhuvaneswari, J. Liu, W. Xu, W. Wang, Z. Yang, G. L. Graff and J.-G. Zhang, *Energy Environ. Sci.*, 2011, **4**, 4560.
3. Y. K. Sun, S. T. Myung, B. C. Park, J. Prakash, I. Belharouak and K. Amine, *Nat. Mater.*, 2009, **8**, 320.
4. S. Nishimura, G. Kobayashi, K. Ohoyama, R. Kanno, M. Yashima and A. Yamada, *Nat. Mater.*, 2008, **7**, 707.
5. L.-X. Yuan, Z.-H. Wang, W.-X. Zhang, X.-L. Hu, J.-T. Chen, Y.-H. Huang and J. B. Goodenough, *Energy Environ. Sci.*, 2011, **4**, 269.
6. N. S. Choi, Z. Chen, S. A. Freunberger, X. Ji, Y. K. Sun, K. Amine, G. Yushin, L. F. Nazar, J. Cho and P. G. Bruce, *Angew. Chem. Int. Ed.*, 2012, **51**, 9994.
7. V. Aravindan, J. Gnanaraj, Y.-S. Lee and S. Madhavi, *J. Mater. Chem. A*, 2013, **1**, 3518.
8. D. B. Ravnsbaek, K. Xiang, W. Xing, O. J. Borkiewicz, K. M. Wiaderek, P. Gionet, K. W. Chapman, P. J. Chupas and Y. M. Chiang, *Nano Lett.*, 2014, **14**, 1484.
9. S. M. Oh, S. W. Oh, C. S. Yoon, B. Scrosati, K. Amine and Y. K. Sun, *Adv. Funct. Mater.*, 2010, **20**, 3260.
10. M. Yonemura, A. Yamada, Y. Takei, N. Sonoyama and R. Kanno, *J. Electrochem. Soc.*, 2004, **151**, A1352.
11. L. Wang, F. Zhou and G. Ceder, *Electrochem. Solid-State Lett.*, 2008, **11**, A94.
12. L. F. J. Piper, N. F. Quackenbush, S. Sallis, D. O. Scanlon, G. W. Watson, K. W. Nam, X. Q. Yang, K. E. Smith, F. Omenya, N. A. Chernova and M. S. Whittingham, *J. Phys. Chem. C*, 2013, **117**, 10383.
13. C. Delacourt, L. Laffont, R. Bouchet, C. Wurm, J. B. Leriche, M. Morcrette, J. M. Tarascon and C. Masquelier, *J. Electrochem. Soc.*, 2005, **152**, A913.
14. D. Morgan, A. Van der Ven and G. Ceder, *Electrochem. Solid-State Lett.*, 2004, **7**, A30.
15. D. Choi, D. Wang, I.-T. Bae, J. Xiao, Z. Nie, W. Wang, V. V. Viswanathan, Y. J. Lee, J.-G. Zhang, G. L. Graff, Z. Yang and J. Liu, *Nano Lett.*, 2010, **10**, 2799.
16. R. Malik, D. Burch, M. Bazant and G. Ceder, *Nano Lett.*, 2010, **10**, 4123.
17. H. Yoo, M. Jo, B.-S. Jin, H.-S. Kim and J. Cho, *Adv. Energy Mater.*, 2011, **1**, 347.
18. W. Shi, S. Song and H. Zhang, *Chemical Society reviews*, 2013, **42**, 5714.
19. X. Rui, X. Zhao, Z. Lu, H. Tan, D. Sim, H. H. Hng, R. Yazami, T. M. Lim and Q. Yan, *ACS Nano*, 2013, **7**, 5637.
20. X.-L. Wu, Y.-G. Guo, J. Su, J.-W. Xiong, Y.-L. Zhang and L.-J. Wan, *Adv. Energy Mater.*, 2013, **3**, 1155.
21. O. Clemens, M. Bauer, R. Haberkorn, M. Springborg and H. P. Beck, *Chem. Mater.*, 2012, **24**, 4717.
22. C. Hu, H. Yi, H. Fang, B. Yang, Y. Yao, W. Ma and Y. Dai, *Electrochem. Commun.*, 2010, **12**, 1784.
23. S.-M. Oh, S.-W. Oh, C.-S. Yoon, B. Scrosati, K. Amine and Y.-K. Sun, *Advanced Functional Materials*, 2010, **20**, 3260.
24. V. Ramar and P. Balaya, *Physical chemistry chemical physics : PCCP*, 2013, **15**, 17240.
25. X. Zhou, Y. Xie, Y. Deng, X. Qin and G. Chen, *J. Mater. Chem. A*, 2015, **3**, 996.
26. H. Wang, Y. Yang, Y. Liang, L. F. Cui, H. S. Casalongue, Y. Li, G. Hong, Y. Cui and H. Dai, *Angew. Chem.*, 2011, **123**, 7502.
27. Z.-X. Chi, W. Zhang, X.-S. Wang, F.-Q. Cheng, J.-T. Chen, A.-M. Cao and L.-J. Wan, *J. Mater. Chem. A*, 2014, **2**, 17359.
28. M.-S. Kim, J.-P. Jegal, K. C. Roh and K.-B. Kim, *J. Mater. Chem. A*, 2014, **2**, 10607.
29. Y. K. Sun, S. M. Oh, H. K. Park and B. Scrosati, *Adv. Mater.*, 2011, **23**, 5050.
30. S. K. Martha, J. Grinblat, O. Haik, E. Zinigrad, T. Drezen, J. H. Miners, I. Exnar, A. Kay, B. Markovsky and D. Aurbach, *Angew. Chem. Int. Ed.*, 2009, **48**, 8559.
31. S.-L. Yang, R.-G. Ma, M.-J. Hu, L.-J. Xi, Z.-G. Lu and C. Y. Chung, *J. Mater. Chem.*, 2012, **22**, 25402.
32. C. Sun, S. Rajasekhara, J. B. Goodenough and F. Zhou, *J. Am. Chem. Soc.*, 2011, **133**, 2132.
33. B. Ding, P. Xiao, G. Ji, Y. Ma, L. Lu and J. Y. Lee, *ACS Appl. Mater. Interfaces*, 2013, **5**, 12120.
34. K. S. W. Sing, *Pure Appl. Chem*, 1985, **57**, 603.
35. H. Liu, F. C. Strobridge, O. J. Borkiewicz, K. M. Wiaderek, K. W. Chapman, P. J. Chupas and C. P. Grey, *Science*, 2014, **344**, 1252817.
36. P. Zuo, G. Cheng, L. Wang, Y. Ma, C. Du, X. Cheng, Z. Wang and G. Yin, *J. Power Sources*, 2013, **243**, 872.
37. H. Yao, G. Zheng, W. Li, M. T. McDowell, Z. Seh, N. Liu, Z. Lu and Y. Cui, *Nano Lett.*, 2013, **13**, 3385.
38. C. Wang, Y. Bi, Y. Liu, Y. Qin, Y. Fang and D. Wang, *J. Power Sources*, 2014, **263**, 332.
39. K. Kisu, E. Iwama, W. Onishi, S. Nakashima, W. Naoi and K. Naoi, *J. Mater. Chem. A*, 2014, **2**, 20789.
40. X. Zhou, Y. Deng, L. Wan, X. Qin and G. Chen, *J. Power Sources*, 2014, **265**, 223.
41. Y. Mi, P. Gao, W. Liu, W. Zhang and H. Zhou, *J. Power Sources*, 2014, **267**, 459.

42. H. Guo, C. Wu, J. Xie, S. Zhang, G. Cao and X. Zhao, *J. Mater. Chem. A*, 2014, **2**, 10581.
43. Y. Zhang, N. Zhang, Z. R. Tang and Y. J. Xu, *Phys. Chem. Chem. Phys.*, 2012, **14**, 9167.
44. S.-Y. Chung, Y.-M. Kim and S.-Y. Choi, *Adv. Funct. Mater.*, 2010, **20**, 4219.
45. L. Wang, P. Zuo, G. Yin, Y. Ma, X. Cheng, C. Du and Y. Gao, *J. Mater. Chem. A*, 2015, **3**, 1569.
46. A. Gutierrez, R. Qiao, L. Wang, W. Yang, F. Wang and A. Manthiram, *Chem. Mater.*, 2014, **26**, 3018.
47. X. Tao, J. Wang, Z. Ying, Q. Cai, G. Zheng, Y. Gan, H. Huang, Y. Xia, C. Liang, W. Zhang and Y. Cui, *Nano Lett.*, 2014, **14**, 5288.